Measurement of the lithographic point-spread function of a focused helium ion beam in negative-tone PMMA and fullerene resists on ultrathin membranes

R. O'Meara[1], V. Dhyani[1], B. R. Tak[1], A. McClelland[2], G. Dawson[2], C. Storey[2], A. P. G. Robinson[3], B. Holst[4], and R. G. Hobbs[1]

[1]Centre for Research on Adaptive Nanostructures and Nanodevices (CRANN) and the SFI Advanced Materials and Bio-Engineering Research Centre (AMBER), Dublin 2, Ireland; School of Chemistry, Trinity College Dublin, The University of Dublin, Dublin 2, Ireland

[2]Irresistible Materials Ltd, Birmingham Research Park, Birmingham, UK

[3]School of Chemical Engineering, University of Birmingham, Edgbaston, Birmingham, B15 2TT, UK

[4]Department of Physics and Technology, University of Bergen, Allégaten 55, 5007 Bergen, Norway

email: hobbsr@tcd.ie

1 Abstract

Helium-ion-beam lithography has many advantages relevant to the fabrication of dense arrays of nanostructures such as a small probe size, large depth of field, and reduced proximity effect. Here, we calculate and measure the lithographic point-spread functions (PSFs) of 30 keV He^+ ions in negative-tone polymethyl methacrylate (PMMA) and a fullerene-derivative resist on ultrathin silicon nitride membranes and compare the results to similar work by Manfrinato *et al.*[1] measuring the PSF of 200 keV electrons in PMMA using an aberration-corrected scanning transmission electron microscope (STEM). PSFs were calculated using the method reported previously by Winston *et al.*[2] Our results show that both the He^+ ion/PMMA and He^+ ion/fullerene-derivative resist PSFs decay more rapidly with distance, r, from the point of incidence of the beam than the corresponding aberration-corrected electron beam/PMMA PSF. In fact, the He^+ ion PSFs decay approximately with r^{-4} while the aberration-corrected EBL PSF decays approximately with r^{-2}. This result implies that the lateral area exposed by the focused beam increases more rapidly with dose for e^- beams than He^+ beams. Effectively, this should result in reduced proximity effect in helium-ion-beam lithography. This work provides further evidence that HIBL offers distinct advantages over EBL for high-resolution and high-density patterning as well as highlighting some benefits of the fullerene-derivative resist over PMMA.

2 Introduction

Helium-ion-beam lithography (HIBL) offers significant advantages over electron-beam lithography (EBL) for fabrication of dense arrays of nanostructures. The helium-ion microscope offers a beam diameter as small as 0.25 nm, and lower beam-convergence angle at the sample than an electron beam of equivalent energy in an electron microscope.[3,4] Thus He^+ ion beams have a larger depth of field than electron beams having equivalent kinetic energy.[3–6] The slower velocity and larger mass of He^+ ions relative to electrons of equivalent kinetic energy results in increased interaction strengths with matter giving He^+ ions larger secondary electron (SE) yields, thus allowing more efficient lithographic exposure.[7–9] He^+ ion beams also exhibit a reduced

proximity effect relative to electron beams of equivalent energy.[10]

Close to the sample surface, He^+ ion beams typically exhibit lower scattering angles relative to electron beams of equivalent kinetic energy.[11] For example, Cohen-Tanugi *et al.*[12] estimated an interaction radius of 1 nm for 30 keV He^+ ions at a depth of 10 nm beneath the surface of a silicon substrate. For electrons and Ga^+ ions of the same energy, the interaction radii at this depth were 2 nm and 15 nm respectively. While the interaction radius of 30 keV electrons is similar to that of He^+ ions, secondary electrons (SEs) are still generated beyond this radius. This is because SEs can be generated via multiple direct and indirect pathways. SE1s, are generated directly by inelastic scattering of the incident beam close to the sample surface.[13] There are multiple routes for the indirect production of type-2 SEs (SE2s). One mechanism for SE2 generation is via inelastic backscattered particles as they return toward the sample surface. A second mechanism is the generation of SE2s by SE1s, however, given the low energy of SE1s generated in helium-ion microscopy, this mechanism can be considered negligible.[14] A third route to SE2 generation is via recoil of atoms in the sample following interaction with an incident energetic particle. Recoiling atoms can kinetically excite electrons provided that the atom velocity is greater than the Fermi velocity of electrons in the target.[14] Moreover, electron energy-loss spectroscopy studies of the interaction of energetic electron beams with resist layers have suggested that volume plasmons play a role in lateral energy spread in EBL resists via the production of SEs at radial locations of up to 10 nm from the incident beam.[15] The lower velocity of helium ions relative to electrons of the same kinetic energy may mean that electrons in the resist can respond to screen the charge of a slow moving helium ion thus reducing the probability of plasmon excitation.[16] Ramachandra *et al.*[17] performed numerical calculations to determine the SE2:SE1 ratio for a range of materials and found that a higher ion energy (>10 keV) yields a lower SE2:SE1 ratio, and thus yields higher resolution. The escape depth, λ_d, of SEs is material dependent. Ramachandra *et al.*[17] calculated λ_d for the interaction of He^+ ions with a wide range of elemental targets and found values of λ_d typically fell in the range 0.75-1.2 nm. SEs generated by the He^+ ion beam thus escape from a volume within approximately 1 nm of the point of incidence of the beam. In an electron beam, SE2s can be generated micrometres away from the incidence beam. Consequently, in

EBL one can expect resist exposure over an area significantly greater than the area of the probe.[11,18]

A point spread function (PSF) describes the response of an imaging system to a point source of radiation. In the case of HIBL and EBL, the lithographic PSF describes how energy from the incident beam is distributed laterally in the resist.[8,15] An accurate description of the PSF for HIBL and EBL is particularly important for the fabrication of dense arrays of nanostructures. Overlapping dose tails of neighbouring point exposures can result in unwanted exposure of regions between directly exposed features (proximity effect). Thus, an accurate description of the PSF can determine how closely printed structures can be resolved and can also be used to calculate corrections for the local dose when patterning smaller features such as sharp points or small gaps, which are desirable features in tunnel junction devices and plasmonic systems for example.[19–22]

In recent decades, nanofabrication on freestanding ultrathin membranes has gained significant interest. The ability to fabricate nanostructures on ultrathin membranes is key to a variety of emerging research fields such as matter wave optics and mask-based matter wave lithography and microscopy.[23–27] Fabrication of nanostructures and nanoscale devices on ultrathin membranes enables characterization of these materials and devices with atomic-scale resolution by (scanning) transmission electron microscopy ((S)TEM) techniques including atomically-resolved imaging, electron energy-loss spectroscopy and energy-dispersive X-ray analysis. TEM techniques are important for the development of plasmonic nanostructures,[28,29] nanoelectronic devices,[30] quantum devices,[31,32] nanopores for DNA sequencing[33] and they enable atomic-scale characterization of nanomaterials such as catalysts.[34] To date, TEM has been used to directly visualise the interaction volume of a He^+ beam in hydrogen silsesquioxane (HSQ) resist on 20-nm-thick SiN_x membranes.[35,36] To our knowledge, similar work using polymethyl methacrylate (PMMA) as a resist has not been conducted, nor has a direct comparison to high-resolution aberration-corrected EBL.

Fabrication on ultrathin membranes reduces scattering of ions or electrons by the substrate, thus reducing the proximity effect and allowing for higher lithographic resolution. EBL has been performed previously on ultrathin membranes using

aberration-corrected STEM.[1,15,37] A high beam energy, $\sim$ 200 keV, results in reduced scattering angles, leading to reduced proximity effects, while a spot size of 0.15 nm, effectively eliminates the beam diameter as a factor limiting resolution. The advanced optics of aberration-corrected STEM, and the use of an ultrathin membrane, minimises scattering in the resist-substrate stack. This approach has been used to determine the ultimate resolution of EBL.[1,15,37] Ultrathin membranes are also of benefit for HIBL, because in addition to reduced scattering by a thinner substrate, most He^+ ions that become embedded in the sample do so at a depth of $>$100 nm below the surface.[38] Consequently, by fabricating features on thin substrates, damage due to helium accumulation can be avoided, and SE generation in the substrate can be minimised. This should further reduce the proximity effect, and help reduce any defects in fabrication caused by damage to the sample, potentially allowing for the ultimate resolution of HIBL to be explored. Here, we compare the resolution limits of HIBL with negative-tone PMMA and fullerene-derivative resists on ultrathin membranes to previous reports of the resolution limits of aberration-corrected EBL with negative-tone PMMA on ultrathin SiN_x.[1,15]

Recently, molecular resists, in particular fullerene derivatives, have gained attention for extreme ultraviolet (EUV) and charged-particle lithography.[10,39] Rao *et al.,* found that irradiating fullerene C_{60} films with visible or ultraviolet light resulted in cross-linking of molecules in the film and a reduction in solubility in toluene.[40] Tada *et al.,* were the first to describe fullerene's use as an EBL resist, and subsequently there was a push to develop new negative-tone fullerene-based resists.[10,39,41,42] The exposure mechanism of fullerene derivatives is thought to involve the fragmentation of the fullerene cage, followed by cross-linking of the remaining fragments to form an insoluble deposit. The small molecular size of these resists ($\sim$ 0.7 nm) leads to the expectation that the fragmentation of the resist during exposure will yield smaller feature sizes and reduced line edge roughness (LER).[10,43] To date, sub-10 nm features have been achieved in fullerene derivative resists using HIBL.[10,42] Furthermore, owing to their high carbon content, fullerene-derivative resists have demonstrated high etch resistance.[44] Fullerene derivatives are therefore an attractive candidate for next generation lithography processes.

In this work, we calculate the PSF for both PMMA and a fullerene-derivative resist on thin SiN_x membranes (5-nm thick), and compare the calculated PSFs to experimental results. Winston *et al.* developed a model to calculate the HIBL PSF for HSQ on bulk silicon substrates.[2] In the model, the simulation software *Stopping and Range of Ions in Matter* (SRIM) is used to simulate the trajectories of incident ions in a sample.[45] A schematic depicting the interaction of He^+ ions with the sample is shown in Figure 1. The incident beam is scattered at random scattering sites and initial position, direction, and energy of SEs generated by the incident ions are determined using a Poisson process that traces along the He^+ ion trajectories.[46,47] The SE trajectories were calculated using a Monte Carlo method developed previously for EBL.[47] Finally, the model returns the spatial distribution of energy deposited in the sample.

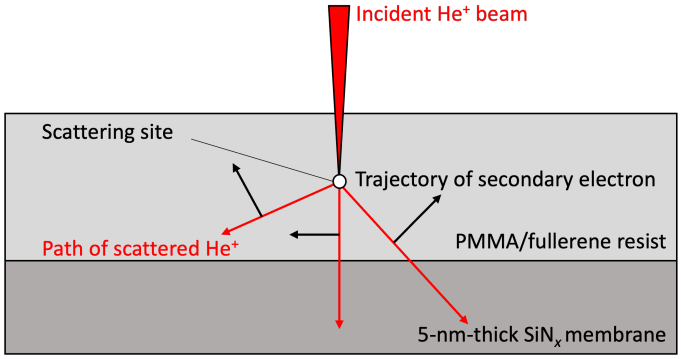

Figure 1: Schematic of interaction of He^+ ion beam with the sample. Red arrows indicate the path of scattered He^+ ions. Black arrows indicate the trajectories of SEs generated by He^+ ions. The beam is scattered in various directions by the sample. SEs are generated with paths perpendicular to the beam at points along the path of a He^+ ion.

3 Experimental

PMMA (1 wt.% 950k molecular weight) in anisole was spin coated at 5 krpm (PMMA thickness $\sim$ 25 nm) onto 3-mm-diameter Si discs containing 50 µm $\times$ 50 µm windows of freestanding ultrathin 5-nm-thick SiN_x (5-nm-thick SiN_x membranes were purchased from *SiMPore Inc.*). Coated discs were baked at 180 °C on a hotplate to remove anisole solvent and relieve film stress. Fullerene-derivative resist in cyclohexanone (HM120, *Irresistible Materials Ltd.*) was spin coated at 5 krpm onto ultrathin 5-nm-thick SiN_x membranes and baked on a hotplate at 70 °C for 5 mins,

yielding a resist thickness of approximately 15 nm on the SiN_x windows. Experimental PSFs were measured by exposing square arrays of single-pixel exposures at various ion doses using a pitch of 100 nm. Exposures were performed using a *Zeiss Orion NanoFab* with a He^+ ion landing energy of 30 keV. Point exposures were made within a 50 μm writefield using a *Raith Elphy Multibeam* pattern generator. Typical experiments used a beam current of 0.3-1.0 pA, 5 μm aperture, spot number of 4, working distance of 8 mm and a helium pressure of 2×10^{-6} Torr. Ion dose per pixel was varied as shown in the PSF plots included in Figure 3. PMMA samples were developed by immersion in acetone followed by a rinse in isopropyl alcohol and drying under a flow of dry nitrogen. Fullerene-derivative resist was developed by immersion in cyclohexanone for 30 s followed by a rinse in isopropyl alcohol and drying under a flow of dry nitrogen. Exposed structures were characterized by scanning electron microscopy (*Zeiss Supra 40*) and bright-field transmission electron microscopy (*JEOL 2100* operating at 200 keV). A full description of the simulation methods used to calculate the PSF is given by Winston *et al.*[2] In order to calculate the PSF, the escape depth, λ_d, the effective energy required to produce an SE, ϵ, the density, ρ, for both the resist and substrate, and the energy and number of the incident He^+ ions must be specified. Ramachandra *et al.*[17] performed simulations to calculate these parameters for a wide range of elements. Values of λ_d = 10.8 Å and ϵ = 59 eV were used to calculate the PSF for PMMA. These are the values the authors calculated for elemental carbon, and were selected as there is no data available for PMMA or elemental hydrogen or oxygen. Densities of 1.18 g/cm^3, 1.0 g/cm^3, and 3.17 g/cm^3 were used for PMMA, the fullerene-derivative resist, and SiN_x respectively. The authors have measured a density of 1.47 g/cm^3 for the fullerene-derivative resist for much thicker 200-nm-thick films, but simulated He^+ scattering was not observed to vary significantly with density in the 1.0-1.5 g/cm^3 range for the resist materials studied and as such a density of 1.0 g/cm^3 was considered sufficient and was based on data for fullerenol from Vraneš *et al.* as this molecule is similar to the fullerene-derivative resist.[48] The energy of the He^+ ions was set as 30 keV, and the number of ions was 100,000.

4 Results and Discussion

TEM images of negative-tone PMMA and fullerene-derivative structures fabricated via He^+ exposure are shown in Figure 2 (additional images are included in the supporting information). Multiple arrays were fabricated with different exposure doses, while the pitch was typically fixed at 100 nm to avoid proximity effects from neighboring exposures. Figure 2(a) shows negative-tone PMMA features fabricated using a dose of 5.5 aC and a pillar with a radius of 3.2 $\pm$ 0.2 nm is highlighted on the image. Figures 2(b) and 2(c) show images of arrays of point exposures exposed with higher doses of 0.7 fC and 10 fC. Figure 2(d) shows pillars formed in negative-tone fullerene-derivative resist with pillar radii of 3.5 nm, while Figures 2(e) and 2(f) show images of arrays of point exposures exposed with higher doses of 1 fC and 10 fC, respectively. The thickness of the resist structures formed during these exposures was estimated by measuring the length of collapsed negative-tone structures, examples of which are shown in Figures 2(b) and 2(e). The measured pillar lengths using this method were typically in the range of 15-20 nm.

Ellipsometry was also used to measure the thickness of resist films prepared on planar 10 mm $\times$ 10 mm Si substrates under identical spin-coating conditions to those used to coat 3-mm-diameter silicon nitride membrane samples. Measured film thicknesses by ellipsometry were approximately 25 nm for PMMA and 15 nm for the fullerene-derivative resists, respectively. Ellipsometry was not possible directly on the SiN_x membranes due to the small dimensions of the 3-mm diameter TEM grids on which the SiN_x membranes are formed. The observed difference in resist thickness, 25 nm before exposure and 15-20 nm after exposure and development for PMMA, is consistent with expected densification of resist following exposure and loss of resist material during development.[49,50]

The experimentally measured He^+ PSFs for both PMMA and a fullerene-derivative resist are shown in Figure 3 alongside the calculated PSF for each resist. Each experimentally measured data point represents the average of 10-15 measured radii and the associated error bars represent the standard deviation in measured radii for a given dose. The simulation was scaled to the experimental data by equating data points with

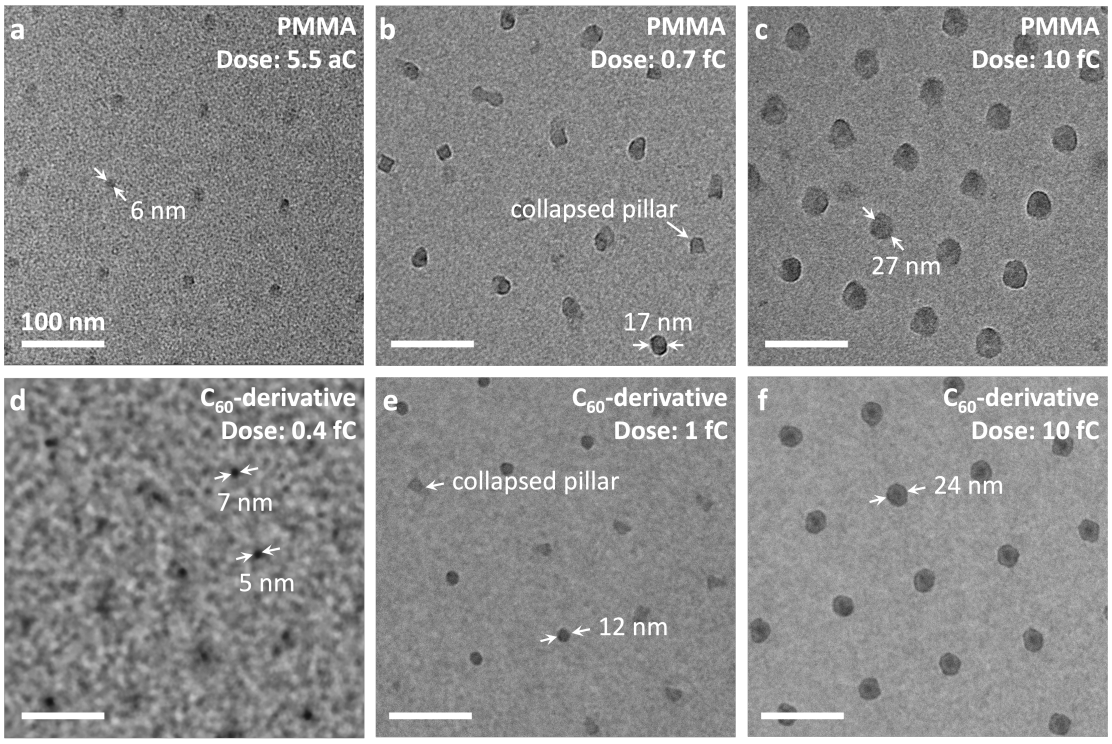

Figure 2: Bright-field TEM images of pillars fabricated in negative-tone PMMA and fullerene-derivative resists. (a-c) TEM images of pillars formed in negative-tone PMMA at single pixel exposure doses of 5.5 aC, 0.7 fC and 10 fC. (d-f) TEM images of pillars formed in negative-tone fullerene derivative resist at single pixel exposure doses of 0.4 fC, 1 fC and 10 fC. Collapsed pillars are visible for each resist in (b) and (e) showing pillar heights in the 15-20 nm range. A pitch of 100 nm was used for all exposures and scale bars represent a length of 100 nm in all images.

$r \sim 12.5$ nm for PMMA and $r \sim 13$ nm for the fullerene resist, as there is a trade-off between experimental uncertainty and statistical uncertainty in the simulation for features of this size as per Winston *et. al.*[2] It can be seen from Figure 3, that the calculated results match well with experiment for both resists. The fitting function below (equation 1) was adapted from the function developed by Winston *et al.* for their simulated data to fit our results.

$$PSF(r) = A((\frac{1}{\sigma_1^2})e^{-(\frac{r}{\sigma_1})^2} + \eta(\frac{1}{\sigma_2^2})e^{-(\frac{r}{\sigma_2})^2}) + Be^{-\frac{r}{r_e}} + C\sqrt{\frac{1}{1+(\frac{r}{r_f})^p}}, \qquad (1)$$

In equation 1, r is the radius of the feature produced at a given dose, σ_1 indicates the beam spot size and lateral extent of forward scattering, and σ_2 represents the lateral extent of backscattering. The exponential term is analogous to Beer-Lambert-like

absorption of SEs with r_e as the mean free path as previously reported.[2] The final term is a filter function featuring a threshold radial value, r_f. When r is less than r_f, the square root term has a value near 1. Consequently, the filter function term effectively sets a minimum exposure dose equivalent in value to C, below which lithographic exposure is not produced. When r exceeds r_f, the value of this function drops off, scaling with a power-dependence defined by the exponential term, p, in the denominator. Table 1 shows the values of parameters from Equation 1 for both resists studied here.

	A	σ_1	η	σ_2	B	r_e	C	r_f	p
PMMA	8×10^4	0.7 nm	0.02	75 nm	2×10^4	0.6 nm	2000	0.5 nm	4
Fullerene-derivative	4500	0.7 nm	0.02	40 nm	8000	0.5 nm	100	0.5 nm	5

Table 1: Parameters for Equation 1. for both PMMA and Fullerene-derivative.

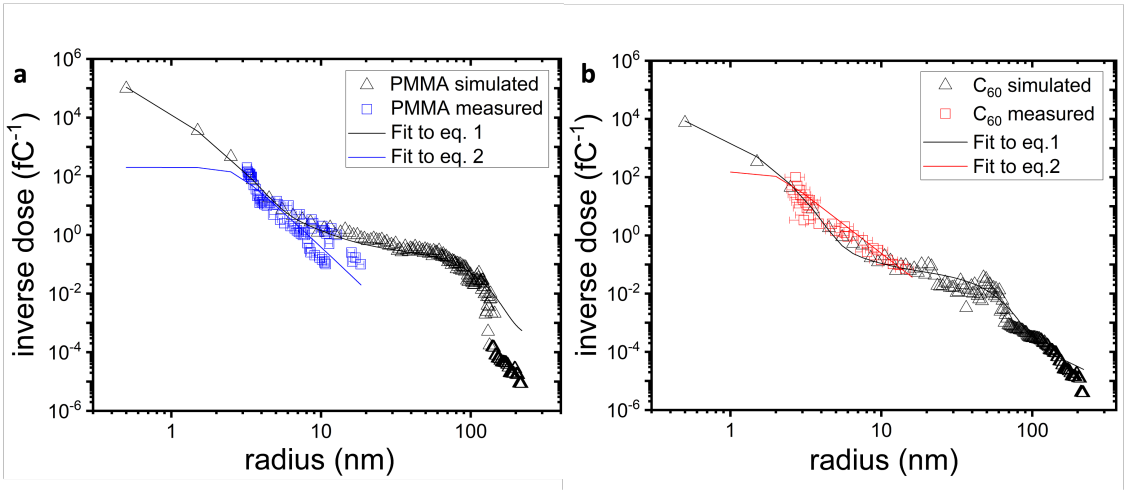

Figure 3: Experimental and simulated PSFs for (a) PMMA and (b) a fullerene-derivative resist on SiN_x, as well as the calculated fitting function to the simulation, and a fit to the experimental data using just a low-pass filter function. The multi-term fitting function was scaled to the experimental data by equating data points with $r \sim 12.5$ nm for PMMA and $r \sim 13$ nm for the fullerene-derivative resist. (a) Blue squares represent average measured radii of 10-15 exposed PMMA pillars for a given dose. Black triangles represent calculated radii of negative-tone PMMA features. The black line represents a fit of equation 1 to the simulated data. The blue line represents a fit of equation 2 to the measured data with r_f = 3 nm. (b) Red squares represent average measured radii of 10-15 pillars of fullerene-derivative for a given dose. Black triangles represent calculated radii of pillars in fullerene-derivative. The black line represents a fit of equation 1 to the simulated data. The blue line represents a fit of equation 2 to the measured data with r_f = 2 nm. Error bars in experimentally measured radii represent 1 standard deviation.

It can be seen from Figure 3 that the dose required for exposure matches well with the model used here and predicts that the inverse dose increases rapidly as the feature

radius drops below approximately 3 nm for both resists. The exposure of features on these short length scales is driven by short-range secondary electrons.[51,52] It is difficult to accurately model the contribution of these short-range SEs as they do not leave the sample by definition. It is possible that smaller feature sizes are achievable, but may not be seen here due to the thickness of the resist layer. As exposure by He^+ ions is highly surface sensitive, it is possible that for low doses, the region near the surface of the resist layer is receiving enough dose to allow for sufficient cross-linking to form negative-tone structures, but that this exposure does not extend fully through the entire thickness of the resist layer. Consequently, when the unexposed resist is removed by the developer, these features are washed away. The thickness of each resist was estimated to be $\sim$25 nm and $\sim$15 nm for PMMA and fullerene-derivative resist, respectively, prior to exposure. It is possible that with the use of a thinner resist layer smaller feature sizes could be achieved, however, we were unable to generate uniform films with thickness below 15 nm in this work due to the challenges associated with spin coating 3 mm diameter chips. Moreover, as can be seen in Figure 2, thinner structures such as the collapsed pillars, exhibit lower contrast in TEM images and are more challenging to measure. The model given by equation 1 predicts that smaller features could be produced by reducing the dose to lower values than those presented in Figure 3 and there is some evidence to support this prediction in our work. For example, Figure S4 shows a TEM image of an array of negative-tone PMMA dots exposed at a pitch of 30 nm and narrow bridges of exposed material are observed between dots due to the proximity effect at the doses used (10 aC per dot). Some of these bridging structures have widths in the range of 2-4 nm, which would be equivalent to dot radii of 1-2 nm in a PSF plot. These small bridging features remain for the case of dense 30-nm-pitch dots as they are supported by the larger dots from which they are supported. However, in practice for quasi-isolated dots *e.g.* 100-nm pitch, there was a minimum dose at which exposed pillar structures yielded. Consequently, we also consider a model described solely by the third term of equation 1, the filter function, which as stated above effectively defines a dose threshold for exposure.

The experimental data was also fitted to the filter function in equation 2, as per

previous work by Manfrinato *et al.*[1]

$$PSF(r) = A\sqrt{\frac{1}{1+(\frac{r}{r_f})^b}} \tag{2}$$

The value of *A* is related to the lowest dose at which features yielded, while the value of r_f is the radius of the PSF and effectively defines the smallest feature size that can be formed. The single term fitting function in equation 2 is believed to be a better choice for this data than the multi-term function in equation 1 as it provides a good fit to the experimental data while also being much simpler than equation 1. As shown in Figure 3, equation 1 implies that features with dimensions approaching 0.1 nm may be resolvable at the lowest doses. However, the model does not account for the quantized nature of ions used for exposure *i.e.,* the minimum possible dose is that of a single ion exposure at $\sim 10^{-19}$ C ($\sim 10^4$ fC^{-1}). Furthermore, in practice, as the dose approaches the level of a single-ion exposure, shot noise from the He^+ source will begin to dominate and limit the practical production of features having reproducible sizes due to fluctuations in the dose delivered. Equation 2 allows a threshold dose and minimum feature size to be defined, which is more representative of what is observed experimentally. Using this function also allows us to compare our results for each resist directly with each other as well as the results from the aberration-corrected EBL work by Manfrinato *et al.*[1]

Figure 4 compares the experimental data from this work to the 2017 report of Manfrinato *et al.*[1] based on a similar PMMA-SiN_x system, using an aberration-corrected STEM. In their work, the smallest negative-tone PMMA structures fabricated had a radius of 0.85 nm, while the smallest pitch obtained for negative-tone PMMA structures was 10.7 nm. The aberration-corrected EBL work used an accelerating voltage of 200 keV, and the dose required to pattern 6-nm diameter features was approximately 100-1000 fC. In contrast, the doses required to pattern 6-nm diameter features by HIBL in this work were in the 0.01-0.1 fC range. This corresponds to $\sim 10^4$ times difference in the sensitivity between exposure with a 30 keV He^+ ion beam and a 200 keV electron beam. For He^+ ion and electron exposures of PMMA at 30 keV, a sensitivity gain of 116 for He^+ ions has been previously reported by van der

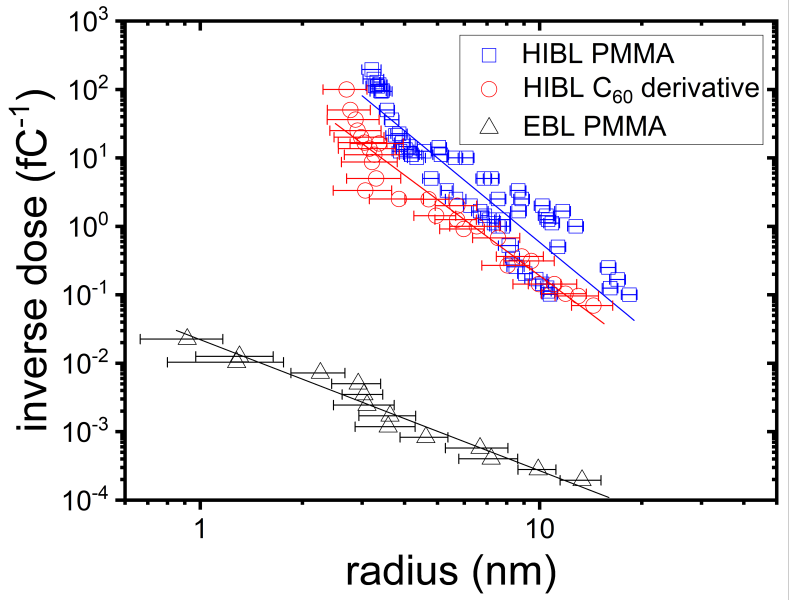

Figure 4: Comparison between experimental data from this work using helium-ion beam lithography and experimental data from the work of Manfrinato *et al.* using electron-beam lithography in an aberration-corrected STEM. The fitting lines represent power-law fits to each PSF. The blue fit for HIBL PMMA represents scaling with radius, r, proportional to $r^{-4.1}$, the red fit for HIBL C_{60} derivative scales with $r^{-3.7}$ and the black fit for aberration-corrected EBL with PMMA scales with $r^{-1.9}$.

Drift *et al.* for negative-tone PMMA on bulk substrates.[53] Similar work by Shi *et al.* showed that 30 keV He^+ ions required a 500 times lower dose than 30 keV electrons for exposure of a fullerene-derivative resist.[10] In the aberration-corrected EBL work by Manfrinato *et al.*, an accelerating voltage of 200 kV was used and as such a much higher dose is expected than for the case of a 30 keV electron due to the longer inelastic mean free path of the more energetic electron. Therefore, while van der Drift *et al.* have reported a difference in sensitivity of 116 times when comparing 30 keV electrons to 30 keV helium ions for negative-tone PMMA exposure on a bulk substrate, a larger difference is to be expected in the comparison of 200 keV electrons to 30 keV helium ions due to the longer inelastic mean free path of the 200 keV electron and because here we are considering point exposures on ultrathin membranes, as opposed to area exposures on bulk substrates as reported by van der Drift *et al.*[53]

A PSF with a large negative slope indicates that the energy deposited in the resist falls off quickly with increasing radial distance from the point of exposure *i.e.,* there is a reduced proximity effect. Consequently, there will be greater dose contrast between

two closely-spaced structures. It can be seen from Figure 4 that the PSFs for PMMA and the fullerene-derivative resist exposed by HIBL exhibit similar scaling with dose. The fullerene-derivative resist requires a slightly larger dose than PMMA to produce features with the same radii, which may present a slight advantage over PMMA because shot noise can become an issue for consistent fabrication at low doses. Consequently, the higher doses required for the fullerene-derivative resist may help to mitigate some of the problems introduced by patterning at very low doses. When comparing the HIBL results from this work to the data from the aberration-corrected EBL work, it can be seen that both resists exposed with a He^+ ion beam have significantly steeper PSF slopes than the corresponding PSF for the electron-beam exposure on PMMA. Specifically, the He^+ ion PSFs decay approximately with r^{-4}, while the aberration-corrected EBL PSF decays approximately with r^{-2}, where r is the radial distance from the point of exposure. Manfrinato *et al.* in their 2013 paper have previously reported that aberration-corrected EBL with a 200 keV beam produces a steeper PSF than EBL with a 30 keV beam and indicated that aberration-corrected EBL at 200 keV represented the state of the art in terms of EBL resolution and contrast.[37] The observation here that HIBL can achieve a steeper PSF than aberration-corrected EBL confirms one of the major benefits of HIBL over EBL, that being the reduced proximity effect exhibited by HIBL due to the steeper PSF. At present, there are no dedicated HIBL tools in production, but the results here indicate that HIBL supports high density pattern formation and may outperform EBL in the production of ultra high density patterns. The PSFs measured here may be used to predict contrast in high density patterns as discussed below.

Figure 5 shows the dose contrast as a function of exposure pitch, calculated using equation 3 below, for the experimental PSF. Dose contrast, K, is defined as:

$$K = \frac{D_{\text{max}} - D_{\text{min}}}{D_{\text{max}} + D_{\text{min}},} \tag{3}$$

where D_{max} is the dose delivered to the centre of an individual spot in a square array of point exposures, and D_{min} is the dose delivered to a point midway between two spots in the array, as shown in Figure 5(a). Dose contrast provides information about how close to one another features can be fabricated. In order to calculate the dose contrast a

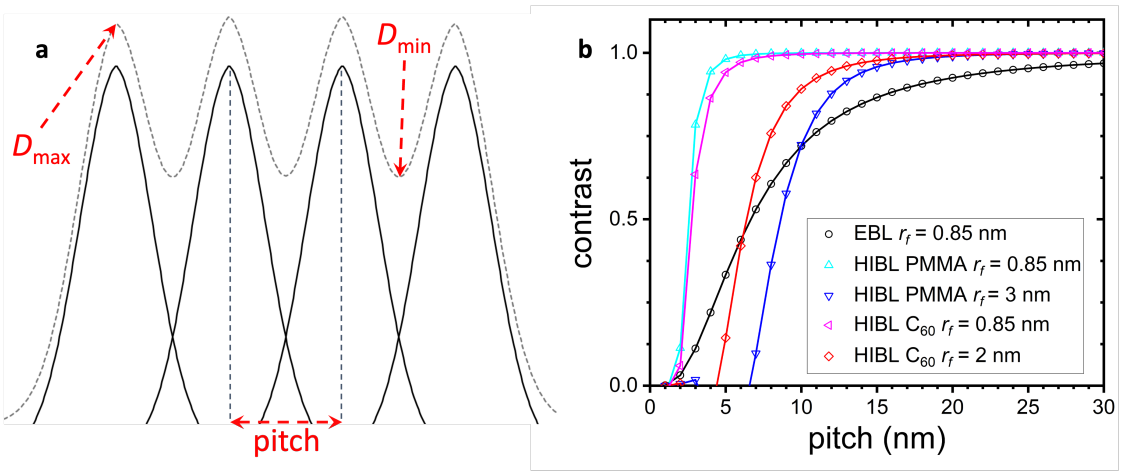

Figure 5: (a) To calculate dose contrast the PSF was used to generate an array of point exposures with a given pitch within a 2 µm × 2 µm area. The dose at any given point is equivalent to the sum of all doses from each point exposure. D_{max} is the total dose experienced at the centre of a single point exposure. D_{min} is the total dose experienced at a point that is equidistant between two independent dose exposures. (b) Plots of dose contrast versus pitch for PMMA on SiN_x calculated using the PSF predicted by Equation 2 for different values of r_f.

MATLAB script was written that first defines a 2 µm × 2 µm writefield consisting of point exposures with a specified pitch. The total dose is calculated at the centre of one point exposure (D_{max}) and at a point midway two point exposures (D_{min}) by evaluating the sum of all PSFs for each point exposure in the array at these locations. Dose contrast, K, can then be calculated using equation 3. A plot of dose contrast versus pitch is shown in Figure 5(b). In the ideal scenario where $K = 1$, the region between two point exposures receives a dose of zero, so both structures can be fabricated with no unwanted indirect exposure of the region between the structures. A value of $K = 0$ corresponds to zero dose contrast whereby D_{max} is equal to D_{min}. The region is overexposed, and thus no structures will be resolved. The true value of the radius of the PSF, r_f, is unknown so here we show the expected contrast for a range of values of r_f. The radius of the incident beam is assumed to be $\sim$ 0.25 nm,[3] however the smallest isolated features fabricated in this work had radii of 3.2 nm for PMMA and 2.7 nm for the fullerene-derivative (example TEM images of pillars with these dimensions can be seen in Figures 2a, 2d, S1 and S2). This indicates that for an exposure with sufficient dose to fabricate a negative-tone feature, the energy deposited by the beam into the resist has a lateral spread that is significantly larger than the radius of the beam. Consequently, it is

expected that the value of r_f is larger than the radius of the beam. The values of r_f used for the experimentally measured HIBL data in this work were 3 nm for PMMA and 2 nm for the fullerene-derivative. These values were used as they are near to the size of the smallest feature produced for each resist and also provided good fits to the experimental data. In the case for the aberration-corrected EBL a beam radius of 0.1 nm was measured, and the smallest feature size produced had a radius of 0.85 nm indicating a value of r_f = 0.85 nm.[1] Based on the fact that the aberration-corrected EBL has both a smaller diameter beam and a lower value of r_f, one might expect the aberration-corrected EBL to yield a higher contrast than HIBL for all pitch values. However, as shown in Figure 5, it can be seen that HIBL is expected to result in higher contrast using PMMA resist for pitches larger than 10 nm (compare blue (HIBL with PMMA r_f = 3 nm) and black (EBL) curves in Figure 5). In fact, with the fullerene-derivative resist, HIBL may exhibit higher contrast down to 6 nm pitch (compare red (HIBL with fullerene r_f = 2 nm) and black (EBL) curves in Figure 5). For further comparison, we have calculated the dose contrast for HIBL with PMMA and fullerene-derivative resist using a value of r_f = 0.85 nm, to allow direct comparison to the aberration-corrected EBL work. Further improvement to HIBL processes *e.g.* preparation of uniform resist thicknesses below 10 nm, could enable more reliable production of smaller features, thus lowering the value of r_f for HIBL. Compared to aberration-corrected EBL with $r_f = 0.85$ nm, HIBL is predicted to yield superior contrast for all pitches below 30 nm for both resists. To date, HIBL has been used to fabricate arrays of nanostructures with pitches as low as 8 nm.[54] The results presented here suggest that HIBL can be further improved to fabricate denser arrays of structures than those previously reported.

5 Conclusions

In conclusion, the PSF for the interaction of 30 keV He^+ ions with PMMA and a fullerene-derivative resist on an ultrathin membrane was calculated and measured experimentally. The model used by Winston *et al.*[2] was modified for thin layers of PMMA and a fullerene-derivative on an ultrathin SiN_x membrane and the resulting PSF

was found to agree well with the experimental PSF that was measured. The fullerene-derivative yielded a minimum feature radius of 2.7 nm compared to 3.2 nm for PMMA, while also requiring higher doses, indicating that the fullerene-derivative could be a better choice as a next generation lithographic resist. The experimental results were compared to previous work using state-of-the-art aberration-correction electron beam lithography using PMMA resist on similar membranes. It was found that exposure of PMMA with 30 keV He^+ ions had a sensitivity $\sim 10^4$ times greater than exposure with 200 keV electrons. Dose contrast calculations predict that for He^+ ion exposure with a PSF radius of 3 nm superior contrast is achievable down to a pitch of 10 nm for both PMMA and a fullerene-derivative when compared to a similar exposure using an aberration-corrected electron beam with a PSF radius of 0.85 nm. When HIBL with a PSF radius of 0.85 nm is considered, our work predicts that HIBL will achieve superior contrast to an aberration-corrected EBL process for all array pitches. As the HIBL setup is also far simpler than the aberration-corrected electron-beam lithography setup, our work suggests that HIBL is a superior choice to EBL for the patterning of dense arrays of nanostructures with pitches in the sub-30-nm regime.

6 Acknowledgements

This work was funded by the European Union's Horizon 2020 Research and Innovation Programme H2020 FETOPEN-2018-2019-2020-01 under Grant Agreement No. 863127 nanoLace (www.nanolace.eu). RGH and ROM acknowledge the support of Science Foundation Ireland (SFI) through The Advanced Materials and Bioengineering Research Centre (AMBER, grant 12/RC/2278_2) and the Royal Society-Science Foundation Ireland University Research Fellowship (15/RS-URF/3306). Access to electron microscopy and lithography equipment was provided through the Advanced Microscopy Laboratory at Trinity College Dublin. The authors acknowledge valuable discussions and technical support from Clive Downing, Dr. Raman Bekarevich and Dr. Riley Gatensby. In particular, the authors wish to acknowledge the support provided by Dr. Raman Bekarevich in acquiring some of the TEM images presented here.

References

[1] Manfrinato, V. R.; Stein, A.; Zhang, L.; Nam, C. Y.; Yager, K. G.; Stach, E. A.; Black, C. T. *Nano Letters* **2017**, *17*, 4562–4567.

[2] Winston, D.; Ferrera, J.; Battistella, L.; Vladár, A. E.; Berggren, K. K. *Scanning* **2012**, *34*, 121–128.

[3] Ward, B. W.; Notte, J. A.; Economou, N. P. *Journal of Vacuum Science & Technology B: Microelectronics and Nanometer Structures* **2006**, *24*, 2871.

[4] Hill, R.; Notte, J.; Ward, B. *Physics Procedia* **2008**, *1*, 135–141.

[5] Flatabo, R.; Agarwal, A.; Hobbs, R.; Greve, M. M.; Holst, B.; Berggren, K. K. *Nanotechnology* **2018**, *29*, 275301.

[6] Guo, H.; Itoh, H.; Wang, C.; Zhang, H.; Fujita, D. *Applied Physics Letters* **2014**, *105*, 023105.

[7] Hill, R.; Notte, J. A.; Scipioni, L. *Advances in Imaging and Electron Physics*; Academic Press Inc., 2012; Vol. 170; pp 65–148.

[8] Winston, D.; Cord, B. M.; Ming, B.; Bell, D. C.; DiNatale, W. F.; Stern, L. A.; Vladar, A. E.; Postek, M. T.; Mondol, M. K.; Yang, J. K. W.; Berggren, K. K. *Journal of Vacuum Science & Technology B: Microelectronics and Nanometer Structures* **2009**, *27*, 2702.

[9] Fallica, R.; Kirchner, R.; Ekinci, Y.; Mailly, D. *Journal of Vacuum Science & Technology B, Nanotechnology and Microelectronics: Materials, Processing, Measurement, and Phenomena* **2016**, *34*, 06K702.

[10] Shi, X.; Prewett, P.; Huq, E.; Bagnall, D. M.; Robinson, A. P.; Boden, S. A. *Microelectronic Engineering* **2016**, *155*, 74–78.

[11] Notte, J.; Ward, B.; Economou, N.; Hill, R.; Percival, R.; Farkas, L.; McVey, S. An introduction to the helium ion microscope. AIP Conference Proceedings. 2007; pp 489–496.

[12] Cohen-Tanugi, D.; Yao, N. *Journal of Applied Physics* **2008**, *104*, 063504.

[13] Ohya, K.; Inai, K.; Nisawa, A.; Itoh, A. *Nuclear Instruments and Methods in Physics Research Section B: Beam Interactions with Materials and Atoms* **2008**, *266*, 541–548.

[14] Hlawacek, G.; Veligura, V.; van Gastel, R.; Poelsema, B. *Journal of Vacuum Science & Technology B, Nanotechnology and Microelectronics: Materials, Processing, Measurement, and Phenomena* **2014**, *32*, 020801.

[15] Manfrinato, V. R.; Wen, J.; Zhang, L.; Yang, Y.; Hobbs, R. G.; Baker, B.; Su, D.; Zakharov, D.; Zaluzec, N. J.; Miller, D. J.; Stach, E. A.; Berggren, K. K. *Nano Letters* **2014**, *14*, 4406–4412.

[16] Baragiola, R. A.; Ritzau, S. M.; Monreal, R. C.; Dukes, C. A.; Riccardi, P. *Nuclear Instruments and Methods in Physics Research Section B: Beam Interactions with Materials and Atoms* **1999**, *157*, 110–115.

[17] Ramachandra, R.; Griffin, B.; Joy, D. *Ultramicroscopy* **2009**, *109*, 748–757.

[18] Bernstein, G. H.; Carter, A. D.; Joy, D. C. *Scanning* **2013**, *35*, 1–6.

[19] Lee, C.-L.; Chien, S.-W.; Tsai, K.-Y. Model-based proximity effect correction for helium ion beam lithography. Novel Patterning Technologies 2018. 2018; p 105841C.

[20] Lee, C.-L.; Chien, S.-W.; Tsai, K.-Y.; Liu, C.-H. *Journal of Micro/Nanopatterning, Materials, and Metrology* **2021**, *20*, 033201.

[21] Putnam, W. P.; Hobbs, R. G.; Keathley, P. D.; Berggren, K. K.; Kärtner, F. X. *Nature Physics* **2017**, *13*, 335–339.

[22] Lee, J.; Jeon, D.-J.; Yeo, J.-S.; Lee, J.; Jeon, D.-J.; Yeo, J.-S. *Advanced Materials* **2021**, *33*, 2006606.

[23] Brand, C.; Sclafani, M.; Knobloch, C.; Lilach, Y.; Juffmann, T.; Kotakoski, J.; Mangler, C.; Winter, A.; Turchanin, A.; Meyer, J.; Cheshnovsky, O.; Arndt, M. *Nature Nanotechnology* **2015**, *10*, 845–848.

[24] Nesse, T.; Simonsen, I.; Holst, B. *Physical Review Applied* **2019**, *11*, 024009.

[25] Palau, A. S.; Eder, S. D.; Bracco, G.; Holst, B. *Ultramicroscopy* **2023**, *251*, 113753.

[26] Cronin, A. D.; Schmiedmayer, J.; Pritchard, D. E. *Reviews of Modern Physics* **2009**, *81*, 1051–1129.

[27] Flatabø, R.; Eder, S. D.; Reisinger, T.; Bracco, G.; Baltzer, P.; Samelin, B.; Holst, B. *Ultramicroscopy* **2024**, *261*, 113961.

[28] Li, Z.; Jin, J.; Yang, F.; Song, N.; Yin, Y. *Nature Communications* **2020**, *11*, 1–11.

[29] Chen, J.; Ye, Z.; Yang, F.; Yin, Y. *Small Science* **2021**, *1*, 2000055.

[30] Korgel, B. A.; Lee, D. C.; Hanrath, T.; Yacaman, M. J.; Thesen, A.; Matijevic, M.; Kilaas, R.; Kisielowski, C.; Diebold, A. C. *IEEE Transactions on Semiconductor Manufacturing* **2006**, *19*, 391–395.

[31] Lehnert, T.; Ghorbani-Asl, M.; Köster, J.; Lee, Z.; Krasheninnikov, A. V.; Kaiser, U. *ACS Applied Nano Materials* **2019**, *2*, 3262–3270.

[32] Tsybeskov, L.; Grom, G. F.; Jungo, M.; Montes, L.; Fauchet, P. M.; McCaffrey, J. P.; Baribeau, J. M.; Sproule, G. I.; Lockwood, D. J. *Materials Science and Engineering: B* **2000**, *69-70*, 303–308.

[33] Liu, S.; Zhao, Q.; Xu, J.; Yan, K.; Peng, H.; Yang, F.; You, L.; Yu, D. *Nanotechnology* **2012**, *23*, 085301.

[34] Su, D. *Green Energy & Environment* **2017**, *2*, 70–83.

[35] Cai, J.; Zhu, Z.; A Alkemade, P. F.; van Veldhoven, E.; Wang, Q.; Ge, H.; Rodrigues, S. P.; Cai, W.; Li, W.-D. *Advanced Materials Interfaces* **2018**, *5*, 1800203.

[36] Deng, Y.; Zhuang, X.; Wang, W.; Gu, R.; He, D.; Wang, L.; Cheng, X. *Nanotechnology* **2021**, *32*, 415302.

[37] Manfrinato, V. R.; Zhang, L.; Su, D.; Duan, H.; Hobbs, R. G.; Stach, E. A.; Berggren, K. K. *Nano Letters* **2013**, *13*, 1555–1558.

[38] Livengood, R.; Tan, S.; Greenzweig, Y.; Notte, J.; McVey, S. *Journal of Vacuum Science & Technology B: Microelectronics and Nanometer Structures* **2009**, *27*, 3244.

[39] Chen, X.; Palmer, R. E.; Robinson, A. P. *Nanotechnology* **2008**, *19*, 275308.

[40] Rao, A. M.; Zhou, P.; Wang, K. A.; Hager, G. T.; Holden, J. M.; Wang, Y.; Lee, W. T.; Bi, X. X.; Eklund, P. C.; Cornett, D. S.; Duncan, M. A.; Amster, I. J. *Science* **1993**, *259*, 955–957.

[41] Tada, T.; Kanayama, T. *Journal of Photopolymer Science and Technology* **1997**, *10*, 647–650.

[42] Yang, D. et al. *Journal of Physical Chemistry Letters* **2022**, *13*, 1578–1586.

[43] Saifullah, M. S.; Rajak, A. K.; Hofhuis, K. A.; Tiwale, N.; Mahfoud, Z.; Testino, A.; Karadan, P.; Vockenhuber, M.; Kazazis, D.; Valiyaveettil, S.; Ekinci, Y. *ACS Nano* **2024**, *18*, 24076–24094, PMID: 39163414.

[44] Manyam, J.; Manickam, M.; Preece, J. A.; Palmer, R. E.; Robinson, A. P. G. Plasma etching of high-resolution features in a fullerene molecular resist. Advances in Resist Materials and Processing Technology XXVIII. 2011; p 79722N.

[45] Ziegler, J. F.; Ziegler, M. D.; Biersack, J. P. *Nuclear Instruments and Methods in Physics Research, Section B: Beam Interactions with Materials and Atoms* **2010**, *268*, 1818–1823.

[46] Joy, D. C. *Monte Carlo modeling for electron microscopy and microanalysis*; Oxford University Press, 1995; p 216.

[47] Ghanbari, R. A. Physics and Fabrication of Quasi-One-Dimensional Conductors. Ph.D. thesis, 1993.

[48] Vraneš, M.; Borišev, I.; Tot, A.; Armaković, S.; Armaković, S.; Jović, D.; Gadžurić, S.; Djordjevic, A. *Physical Chemistry Chemical Physics* **2016**, *19*, 135–144.

[49] Shi, X.; Boden, S. A. In *Materials and Processes for Next Generation Lithography*; Robinson, A., Lawson, R., Eds.; Frontiers of Nanoscience; Elsevier, 2016; Vol. 11; pp 563–594.

[50] Ravi Kiran, N.; Chauhan, M.; Sharma, S. K.; Ghosh, S.; Gonsalves, K. E. *ACS Applied Electronic Materials* **2020**, *2*, 3805–3817.

[51] Rai-Choudhury, P. *Handbook of Microlithography, Micromachining, and Microfabrication. Volume 1: Microlithography*; SPIE PRESS, 1997.

[52] Wu, B.; Neureuther, A. R. *Citation: Journal of Vacuum Science & Technology B: Microelectronics and Nanometer Structures Processing* **2001**, *19*, 2508.

[53] Van Der Drift, E.; Maas, D. J. *Nanofabrication: Techniques and Principles*; Springer-Verlag Wien, 2012; pp 93–116.

[54] Li, W.-D.; Wu, W.; Stanley Williams, R. *Journal of Vacuum Science & Technology B* **2012**, *30*, 06F304.